# Journal of Materials Chemistry A

Accepted Manuscript






ROYAL SOCIETY OF CHEMISTRY

www.rsc.org/materialsA

ARTICLE TYPE www. rsc.org/xxxxxx | XXXXXXXX

# Hydration, oxidation, and reduction of $GdBaCo_2O_{5.5}$ from first-principles.

**Esther Coulaud,[a] Guilhem Dezanneau,[b] and Grégory Geneste*[a]**

Structural, magnetic and chemical properties of $GdBaCo_2O_{5.5}$ regarding hydration, oxidation and reduction, are studied by density-functional calculations in the DFT+*U* formalism. Beside the orthorhombic *Pmmm* structure, a lower energy, tilted, distorted structure is found. The hydrated configurations obtained by water dissociation in the oxygen vacancies of the $GdO_{0.5}$ plane exhibit strong distortions with respect to the *Pmmm* structure. Simulation of protonic defects provides the energy landscape of incorporated protons, that preferentially bind to oxygens of the $CoO_2$ planes, suggesting their possible bidimensional diffusion in this plane. We also study oxygen incorporation (oxidation) in the oxygen vacancies of the $GdO_{0.5}$ planes, and oxygen removal (reduction) from BaO, $CoO_2$ and $GdO_{0.5}$ planes. The oxidized compound, $GdBaCo_2O_{5.75}$, is rather *p*-type metallic, while the reduced compound, $GdBaCo_2O_{5.25}$, remains an insulator, due to electronic localization ($Co^{3+} + e^- \rightarrow Co^{2+}$). Taking *Pmmm* as reference, both hydration at high water concentration (one $H_2O$ per 38-atom supercell), and oxidation are found exothermic. However, if the distorted structure is chosen as reference, these reactions become endothermic, at least at the high water/oxygen concentration studied. Reduction is, in both cases, endothermic. Nevertheless, negative formation energies for the protonic defects suggest possibility of hydration at lower water concentration.

## 1 Introduction

Double perovskite cobaltites of rare earths, with chemical formula $LnBaCo_2O_{5+x}$, are intriguing compounds that exhibit, at low temperatures, a very complex electrical and magnetic behavior, namely temperature-induced insulator/metal and antiferromagnetic/ferromagnetic transitions. In $GdBaCo_2O_{5.5}$ (GBCO), for instance, the insulator/metal transition lies at $\sim$ 360 K[1]. Moreover, at higher temperatures, their structure, which naturally contains a high concentration of oxygen vacancies, is highly favorable to ionic conduction by oxide ion migration[2–10]: the oxygen vacancies, ordered at low temperature along the *a* axis in the $GdO_{0.5}$ plane[11,12], are randomly distributed among the $GdO_{0.5}$ and $CoO_2$ planes at high temperatures. This transition and the corresponding ionic conduction properties have been well described by classical molecular dynamics[13–18] and the high-temperature random state of oxygen vacancies by Monte Carlo simulations[19]. Therefore, these cobaltites can also be used as cathode materials in solid oxide fuel cells (SOFCs), because at the operating temperature of such devices ($>$ 1000 K), they exhibit both electronic and ionic conduction.

However, materials for fuel cells working at lower temperature are desirable. In this respect, solid proton conductors are good candidates because they can play the role of charge (protonic) carriers while working at much lower temperature (typically around 600-900 K). Many perovskites (e.g. $BaZrO_3$, $BaCeO_3$, $BaSnO_3$) doped by elements of lower valence on their B site (e.g. Y, In, Gd in substitution of Zr, Ce, Sn) can be used as electrolytes of such devices, called Protonic Ceramic Fuel Cells (PCFCs). High performance electrodes for PCFCs could be obtained by using mixed proton-electron conductors. This topic is currently being developed with experimental difficulties to identify water incorporation. There is thus some need to be able to anticipate the hydration of potential electrode materials. In this respect, a recent experimental study[20] suggests possible hydration in the GBCO compound, below $\sim$ 340°C. Therefore, we investigate in the present study the ability of GBCO to incorporate water, from first principles density-functional calculations.

In perfect GBCO, all the cobalt ions are $Co^{3+}$ (electronic structure $3d^6$). However, the structure of the compound is favorable to oxygen incorporation (oxidation) in the already present oxygen vacancies. On the other hand, oxygen can be released (reduction) due to the mixed valence of cobalt[21], leading to the appearance of $Co^{2+}$. In these different oxidation states, the very localized 3*d* electrons of Co are subject to strong correlations. The standard approximations to density-functional theory (DFT), such as Local Density Approximation (LDA) or Generalized Gradient Approximation (GGA), are unable to reproduce correctly the strong effect of electrostatic repulsion between the 3*d* electrons of Co. The effect of such repulsion is a splitting of the 3*d* band in two subbands separated by several eV. The so-called DFT+*U* (Hubbard) approach has been shown to successfully overcome this problem in many cobaltites and cobalt oxides. In such systems, the val-

[a] *CEA, DAM, DIF, F-91297 Arpajon, France. E-mail: gregory.geneste@cea.fr*
[b] *Laboratoire Structures, Propriétés et Modélisation des Solides, École Centrale Paris, CNRS-UMR 8580, Grande Voie des Vignes, 92295 Châtenay-Malabry Cedex, France.*

ues of $U$ used to describe the +3 state of Co, either within the LSDA or the GGA, usually range from 5 to 7 eV[22–27] (with $J$ between 0 and 1 eV). Similar values, typically between 4 and 6 eV, are also used for the modeling of the +2 charge state of Co[24,28–30]. In the present work, we will mainly use the GGA+$U$ approximation to the exchange-correlation energy to model the properties of GBCO.

Electronic structure calculations have been performed on GBCO[1,31,32] and related compounds $LnBaCo_2O_{5+x}$[33] in the past years. These calculations have questioned the magnetic state of the $Co^{3+}$ ions, which can be found in octahedral environment under the low-spin (LS) state ($t_{2g}^6 e_g^0$), the intermediate-spin (IS) state ($t_{2g}^5 e_g^1$), or the high-spin (HS) state ($t_{2g}^4 e_g^2$)[22], according to the crystal field intensity compared to the Hund exchange coupling. The LSDA+U calculations of Wu[1], those of Zhang et al.[32] together with a few experimental works[34,35], rather conclude to the HS state. Some experimental studies rather suggest a LS (resp. IS) state for the Co in the octahedral (resp. pyramidal) environment[36–38]. Other studies conclude to HS state for pyramidal Co (related to small crystal field) and a mixture of LS/HS state[18] or simply LS state[39] for octahedral Co. The spin state of the $Co^{3+}$ ions in GBCO is thus still controversial from the experimental point of view.

Taskin et al.[40] investigated the phase diagram of $GdBaCo_2O_{5+x}$, upon varying oxygen stoichiometry as $0 \leq x \leq 0.77$ and gave evidence for a complex electrical and magnetic behavior, in which the oxygen content determines the hole ($p$-type, oxidizing conditions) or electron ($n$-type, reducing conditions) concentration in the $CoO_2$ planes. At low temperature, GBCO is however an antiferromagnetic insulator[40], and remains so on a large range of oxygen concentration, at least in the reduced part. The LSDA+$U$ calculations of Wu[1] show that in the HS configuration, the occupied 3$d$ states of Co are localized deep in the valence band (occupied Hubbard subband). Therefore, the valence band top is mainly made of oxygen 2$p$ states, while the bottom of the conduction band is made of the 3$d$ unoccupied states of cobalt, making the gap of GBCO rather of charge-transfer nature.

In the present work, we employ density-functional calculations in the Hubbard framework to investigate the structure, magnetism, and chemical reactivity of GBCO with respect to hydration, oxidation and reduction. We first model the perfect system and explore possible spin states of Co, possible antiferromagnetic orders and the structure of the compound. A supercell is then used to model $H_2O$, $H^+$, 1/2 $O_2$ insertion, and 1/2 $O_2$ removal, providing trends for the enthalpy of the hydration, oxidation and reduction reactions.

## 2 Computational details

We have performed spin-polarized density-functional theory calculations[41] using the ABINIT code[42,43], in the Projector Augmented-Wave (PAW) framework[44]. Two exchange-correlation functionals have been tested: (i) the Generalized Gradient Approximation as formulated by Perdew, Burke, and Ernzerhof[45], and (ii) in some cases, the Local Spin Density Approximation, both of them augmented by a Hubbard correction on the 3$d$ orbitals of cobalt ($U_{3d}^{Co}$=5 eV, $J_{3d}^{Co}$=0 eV) to account for the localization and strong correlations of the 3$d$ electrons of Co. The robustness of the results concerning the magnetism and the hydration properties have been checked by varying the values of ($U$,$J$), see hereafter. Spin-orbit (SO) coupling is ignored although experiments suggest a strong magnetic anisotropy in GBCO[40]. However, if SO may play a role in subtle magnetic effects related to Co 3$d$ electrons, the effect of electronic correlations is probably much more important and is the phenomenon to correctly account for, thus within DFT+$U$. In the PAW atomic data, we treat as valence electrons the 2$s$ and 2$p$ for oxygen, the 5$s$, 5$p$ and 6$s$ for barium, the 3$s$, 3$p$, 4$s$ and 3$d$ for cobalt.

Our calculations are performed by freezing the 4$f$ electrons of gadolinium in the core of the pseudopotential. This is a way to enforce their localization and prevent them from being involved in the chemical bond[46]. However, we also performed a few calculations by treating the 4$f$ electrons of Gd in the GGA+$U$ framework ($U_{4f}^{Gd}$=5 eV, $J_{4f}^{Gd}$=0 eV) to ensure that the results obtained within this 4$f$ frozen core approximation are robust.

The plane-wave cut-off is 20 Hartrees (convergence tests have been performed up to 30 Ha). Our structural optimizations are performed starting from a 38-atom supercell, whose First Brillouin Zone is sampled by a 3×3×3 $k$-point mesh. The tolerance on the cartesian components of the atomic forces for geometry optimization is $2\times10^{-4}$ Ha/bohr ($\sim$ 0.01 eV/Å), and $2\times10^{-6}$ Ha/bohr$^3$ on components of the stress tensor.

## 3 Pure compound: structure, magnetism, electronic structure

### 3.1 GBCO in the *Pmmm* structure

The structure of GBCO corresponds to a double perovskite structure, with BaO-$CoO_2$-$GdO_{0.5}$-$CoO_2$ planes alternating along the $z$ direction. Oxygen vacancies are ordered in the $GdO_{0.5}$ planes, along the $x$ direction (Fig. 1) and alternate with oxygen rows along $y$. The primitive cell contains 19 atoms and the crystal structure belongs to the orthorhombic *Pmmm* space group[47]. The Co ions in $GdBaCo_2O_{5.5}$ are in the +3 oxidation state. There are two nonequivalent Co: the Co1 are in an octa-

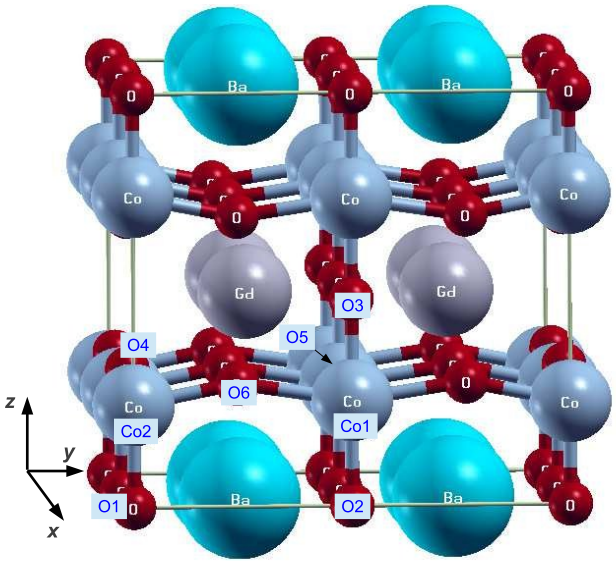


**Fig. 1** Crystal structure of $GdBaCo_2O_{5.5}$ and 38-atom supercell used in the present calculations.

**Table 1** Energies (in eV/perovskite unit cell) of different spin state configurations using $U_{3d}^{Co}$=5 eV, and $J_{3d}^{Co}$=0 or 1 eV (GGA+$U$), within the AFM3 antiferromagnetic order. The energies are referred to the high-spin configuration (HS-HS). n.c.: not calculated; n.o.: not obtained (the calculation has converged to another spin state configuration).

| Spin state of $Co2_{pyr}$ | $Co1_{oct}$ | $Co2_{pyr}$ | (5,0) | (5,1) |
|---|---|---|---|---|
| HS | HS | HS | 0 | 0 |
| | IS | HS | 0.24 | 0.19 |
| | LS | HS | 0.28 | 0.22 |
| | HS/IS | HS | 0.17 | n.o. |
| | HS/LS | HS | 0.11 | 0.13 |
| | LS/HS | HS | 0.11 | 0.08 |
| other spin states | HS | LS | 0.58 | n.c. |
| | IS | LS | n.c. | 0.68 |
| | HS | IS/HS | n.o. | 0.04 |
| | HS | IS | n.o. | 0.03 |
| | LS | LS | 0.91 | 0.81 |

hedral environment, while the Co2 are in a square pyramidal environment. GBCO is observed to be an antiferromagnetic insulator at T=0 K[40].

We use the Kröger-Vink notations to denote the different sites and defects in GBCO. In particular, since the perfect structure naturally contains oxygen vacancies in the $GdO_{0.5}$ planes, these vacancies will be considered as neutral and denoted as $\square_{\square}^{X}$.

First, we have tested 3 possible types of antiferromagnetism in the *Pmmm* structure (AFM1: along $c$, AFM2: along $b$ and $c$, AFM3: along $a$, $b$ and $c$). We have retained the most stable, which corresponds, for $U_{3d}^{Co}$=5 eV and $J_{3d}^{Co}$=0 eV, to AFM3 ($G$-type), the sign of the magnetic moments of Co alternating along the three pseudocubic axis (the energetic order AFM3 < AFM2 < AFM1 is obtained). A 2×2×2 supercell (in terms of the perovskite unit cell) is used to represent this order. This 38-atom AFM3 supercell will be used as starting point for all the structural optimizations in the following sections. These different magnetic structures have been tested using ($U_{3d}^{Co}$,$J_{3d}^{Co}$)=(5,1) and (6,0) eV, with the Gd 4$f$ electrons frozen in the core. The AFM3 structure remains the most stable. In these preliminary calculations, the magnetic moments of the Co ions have been initialized to a value that would correspond to a HS state, and indeed after full structural optimization and convergence of the SCF cycle, the Co are all found in their HS state.

However, we have also tested several kinds of spin states of Co within this AFM3 magnetic order in the *Pmmm* structure (Tab. 1)*. In a first series, we kept the HS state for the pyramidal Co and varied the spin state on the octahedral ones. The most stable of these configurations is a mixture of LS/HS on Co1, which has however an energy higher than the HS-HS state. In a second step, we varied the spin state of the pyramidal Co also. Two configurations are found almost as stable as HS-HS, namely HS-IS and HS-IS/HS (a mixture of IS and HS on the Co2). Nevertheless, among the different configurations studied, the HS-HS is the most stable. Thus in the following, we will consider GBCO as having all its Co in the HS state, i.e. in all the calculations, the magnetic moments of Co are initialized to values typical of the HS state, within the AFM3 order. Note that this is not a constraint of the DFT calculation, just a way to initialize the self-consistent cycles. The HS state will be thus obtained in almost all the cases after structural optimization, except when mentioned.

We now focus on the optimized *Pmmm* structure in AFM3 order, with all the Co ions in HS state. This HS state of the Co ions can be seen on the Co $d$ and O $p$ projected density of states (Fig. 3), namely ($t_{2g}^4$, $e_g^2$), with spin magnetic moments ∼ 3.0 $\mu_B$ (Co1: 3.08, Co2: 3.02). This AFM3 structure is found insulating, with a Kohn-Sham bandgap of ∼ 1 eV (Fig. 2), which is rather of charge-transfer nature, i.e. O 2$p$ → Co 3$d$ (see Fig. 3). Such projected DOS is typical of $Co^{3+}$ in HS state: similar behavior has been observed in $LaCoO_3$ by Knizek et al.[49], who computed the electronic structure of this compound in various spin states for $Co^{3+}$, by Hsu et al.[50], and in $BiCoO_3$[51]. Moreover, these features are in good agreement with the LSDA+$U$ calculations of Wu[1], and with those

* We have not the possibility to constrain the spin state of Co, but with the ABINIT code, there are two ways to favor a certain spin state: (i) initialization of the spin magnetic moment on each Co; (ii) within DFT+$U$, control of the occupation matrices of the correlated orbitals[48].

**Table 2** Theoretical lattice parameters (Å) in $GdBaCo_2O_{5.5}$ (*Pmmm* space group) in the HS-AFM3 state, using several theoretical schemes, and compared to experiments. $J^{Co}_{3d}$=0 eV in the different cases.

| Co 3*d* | Gd 4*f* | a | b | c |
|---|---|---|---|---|
| GGA | | | | |
| $U^{Co}_{3d}$=5 eV | core | 3.945 | 7.991 | 7.595 |
| $U^{Co}_{3d}$=5 eV | $U^{Gd}_{4f}$=5 eV | 3.962 | 8.022 | 7.621 |
| LDA | | | | |
| $U^{Co}_{3d}$=5 eV | core | 3.844 | 7.783 | 7.402 |
| Expt[52] | | 3.87738 | 7.8269 | 7.53487 |
| Expt[53] | | 3.881 | 7.840 | 7.563 |
| Expt[47] | | 3.8760 | 7.822 | 7.533 |

of Zhang et al[32].

In Tab.2 are given the optimized lattice constants for $GdBaCo_2O_{5.5}$ (*Pmmm* space group) in the HS-AFM3 state, using different treatments of the Co 3*d* and Gd 4*f* electrons. As expected, GGA+*U* overestimates the lattice constants. LDA+*U* exhibits the opposite tendency, *i.e.* it underestimates the lattice parameters, as expected also. More information about the structure (atomic positions) and magnetism are given in the Appendix.

Using $(U^{Co}_{3d},J^{Co}_{3d})$=(0,0) eV (pure GGA), GBCO is found, by contrast, metallic even in the AFM state, which contradicts the experiments[40] and confirms the necessity of using DFT+*U* to model this cobaltite. Using now $(U^{Co}_{3d},J^{Co}_{3d})$=(5,0) eV and a full treatment of the 4*f* electrons of Gd in the valence (with $U^{Gd}_{4f}$=5 eV, $J^{Gd}_{4f}$= 0 eV), similar electronic properties are obtained (we assume FM coupling between the Gd). The electronic density of states computed this way is shown on Fig. 2, together with that obtained when the 4*f* electrons are frozen in the core. They are very similar, excepting that the former exhibits the two narrow peaks of opposite spins corresponding to the 4*f* states of the ferromagnetically coupled $Gd^{3+}$ ions.

In the following sections, the results are given for $(U^{Co}_{3d},J^{Co}_{3d})$=(5,0) eV and the Gd 4*f* electrons frozen in the core, except when explicitly mentioned, and the calculations are systematically initialized with the Co magnetic moments arranged according to the AFM3 configuration in HS state.

### 3.2 Distortion from the *Pmmm* structure

The previous calculations have been performed by assuming *Pmmm* as the structure of GBCO. The symmetries of this structure have been thus imposed in all the structural optimizations. However, we released these symmetry constraints, and found a lower-symmetry structure with lower energy. This structure exhibits tilts of the oxygen octahedra around the *z*

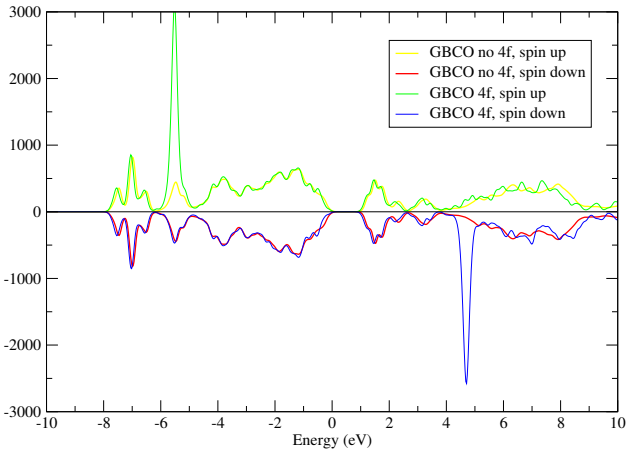


**Fig. 2** Electronic density of states of GBCO (arb. units) in its *Pmmm* structure using (i) a PAW atomic data of Gd with the 4*f* electrons frozen in the core (yellow and red curves), and (ii) a PAW atomic data of Gd with the 4*f* electrons explicitly treated in the valence (green and blue curves). $(U^{Co}_{3d},J^{Co}_{3d})$=(5,0) eV in both cases. $U^{Gd}_{4f}$ = 5 eV in the second case. The Fermi energy is set at 0 eV. The Co ions are antiferromagnetically coupled, but the Gd ions are assumed as ferromagnetically coupled.

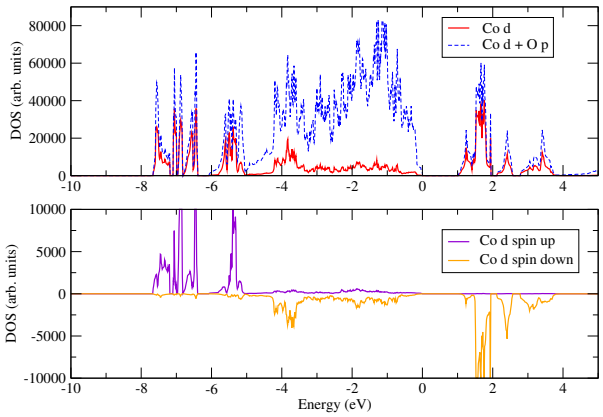


**Fig. 3** Density of states (arb. units) of perfect GBCO (AFM3 magnetic order). Upper panel: projection on *d* states of Co, and sum of Co *d* states and *p* states of oxygen. The two Hubbard subbands are well visible, and separated by $\sim$ 8-9 eV. Lower panel: Projection on Co1 (octahedral environment) *d* states. The majority spin states (up) are completely filled, while the minority spin (down) are incompletely filled, indicating the high-spin state of the $Co^{3+}$ ion ($t^3_{2g,\uparrow}$,$t^1_{2g,\downarrow}$,$e^2_{g,\uparrow}$,$e^0_{g,\downarrow}$). The tetrahedron method is used for the computation of the DOS.

axis, and is found in GGA+$U$ more stable than *Pmmm* by 1.19 eV/38-atom supercell. In LSDA+$U$ with the same $U_{3d}$ and $J_{3d}$, it is 0.61 eV more stable. Fig. 4 shows this tilted structure. Distortions from the *Pmmm* space group, associated with appearance of a superstructure below the metal-insulator transition have already been reported in GBCO[39,54,56], and also in reduced GBCO[55]. Although the precise nature of the distortion remains unclear, the present calculation provides a candidate structure that could be compared to experiments. In this low-energy structure of GBCO, the Co ions are still found in the AFM3-HS state, but no other AFM order nor spin state configuration has been tested.

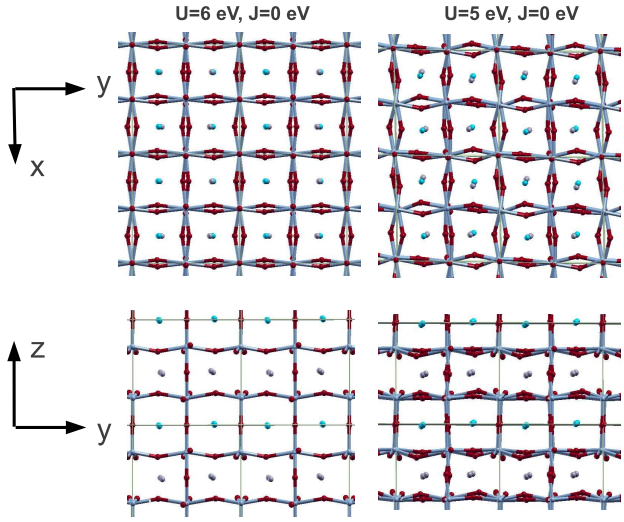


**Fig. 4** Tilted structure of GBCO, optimized with $U_{3d}^{Co}$ = 6 and 5 eV, and $J_{3d}^{Co}$ = 0 eV.

## 4 Hydrated configurations

The hydration reaction in GBCO can be written as

$$H_2O(g) + \square_{\square}^{X} + 2O_O^X \rightarrow 2(OH)_O^{\bullet} + O_{\square}^{''}. \quad (1)$$

It corresponds to a water molecule dissociating in an oxygen vacancy: its oxygen fills the vacancy under the form of an oxide ion, $O_{\square}^{''}$, while the two hydrogens bind to oxygen atoms under the form of hydroxyl groups (protonic defects).

### 4.1 Hydration at high water concentration

In the 38-atom supercell, one oxygen vacancy is therefore filled by a O atom, and two H are added in interstitial positions close to oxygen atoms. Various relative configurations are tested and fully optimized (atomic positions and lattice constants), with the two protons bonded to oxygens of the BaO, $CoO_2$ or $GdO_{0.5}$ planes. For each configuration, the hydration enthalpy is computed according to

$$\Delta H_{hydr} = E_{tot}(GBCO + H_2O) - [E_{tot}(GBCO, ref) + E_{tot}(H_2O)],$$

in which the different terms are, respectively, the total energies of the hydrated supercell (fully optimized, atomic positions and lattice constants), of the dry supercell in the chosen reference structure (either *Pmmm* or the tilted structure previously described), and of the isolated water molecule. Note that inserting one $H_2O$ molecule in the 38-atom supercell corresponds to filling 50% of the oxygen vacancies, leading to a strongly hydrated system, of chemical formula $GdBaCo_2O_{5.75}H_{0.5}$. As a consequence, there is a very large volume increase in the final system (typically around 5%), and the hydration enthalpies thus contain a strong elastic contribution. The two protons are placed, in each plane, as far as possible to minimize their electrostatic repulsion, only the orientation of the OH groups is varied.

The configurations corresponding to the protons in the BaO plane are labelled B1 ... B6. The OH lie in this plane, perpendicular to the Co-O bonds aligned along the $c$ axis. The final optimized geometries are shown on Fig. 5. For the protons bonded to oxygen atoms in the $CoO_2$ plane, 4 configurations have been studied. The first one (C1) corresponds to the OH groups lying in the plane and initially pointing in the y direction. For the second and third configuration, OH groups are perpendicular to the $CoO_2$ plane and point either toward the $GdO_{0.5}$ plane (C2) or toward the BaO plane (C3). In C4, the two OH do not belong to the same $CoO_2$ plane, and both point towards the $GdO_{0.5}$ plane that separates them. The final optimized geometries are shown on Fig. 6. The configurations with the two protons initially placed in the $GdO_{0.5}$ plane are labeled G1 and G2. Other configurations, labeled GC1 and GC2, have one proton in the $GdO_{0.5}$ plane and the other in the $CoO_2$ one. The final optimized geometries are shown on Fig. 7.

The hydration enthalpies in these different configurations are given in Tab.3, with the nature of the two protonic sites involved (labeled by the oxygen to which $H^+$ is bonded followed by direction of the OH group).

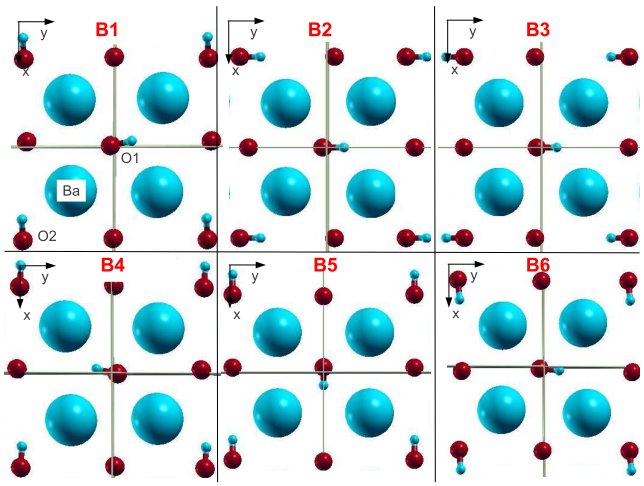


**Fig. 5** View of the optimized hydrated configurations with the two protons bonded to oxygens of the BaO plane. Note that 50% of the oxygen vacancies are filled by the oxygens coming from $H_2O$.

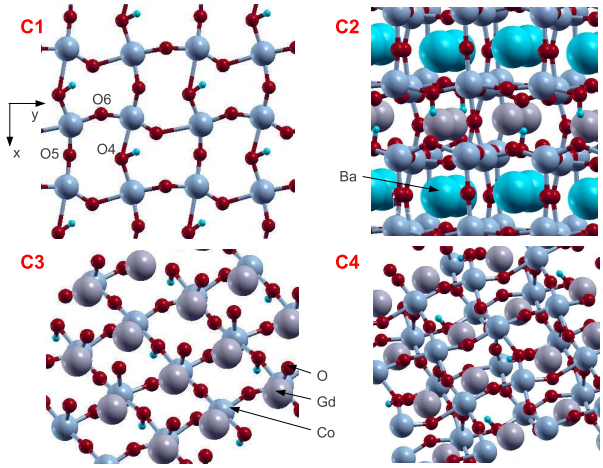


**Fig. 6** View of the optimized hydrated configurations with the two protons bonded to oxygens of the $CoO_2$ planes. Note that 50% of the oxygen vacancies are filled by the oxygens coming from $H_2O$.

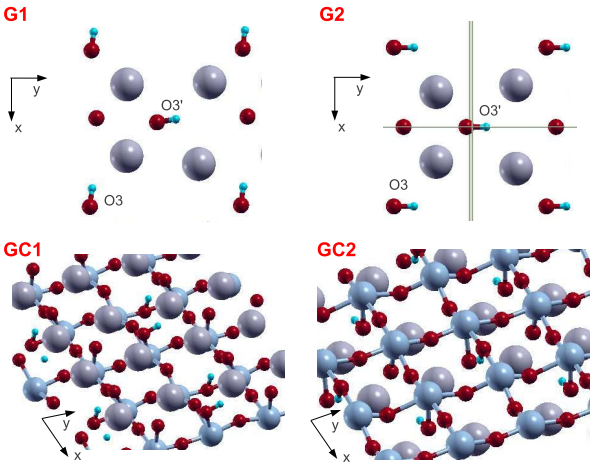


**Fig. 7** View of the optimized hydrated configurations with the two protons bonded to oxygens of the $GdO_{0.5}$ plane, and the ones having one proton in the $GdO_{0.5}$ plane, and the other in the $CoO_2$ plane. Note that 50% of the oxygen vacancies are filled by the oxygens coming from $H_2O$. O3' denotes the oxygen atom added in the $GdO_{0.5}$ plane following water insertion.

Two configurations emerge as more stable than the others: C4 and C1. They have negative hydration enthalpies with respect to *Pmmm* (see Tab.3). They are shown on Fig. 6 and correspond to protons bonded to oxygens of the $CoO_2$ plane(s), either lying in the plane (C1), or perpendicular to it pointing to the $GdO_{0.5}$ plane (C4). In C1 (OH groups lying in the $CoO_2$ plane), the hydration enthalpy is -0.59 eV/$H_2O$ molecule (w/r to *Pmmm*). The structure is strongly distorted. In particular, the $CoO_2$ plane undergoes a strong antiferrodistortion (Fig. 6). In C4 (OH groups perpendicular to the $CoO_2$ plane and pointing to the $GdO_{0.5}$ plane, the hydration enthalpy is -0.63 eV/$H_2O$ molecule (w/r to *Pmmm*), here again with strong structural distortions (Fig. 7).

In the most stable hydrated configuration (C4), the charge state of Co atoms (3+) and the magnetism (AFM3 in high-spin configurations) are not modified by the hydration process. The system remains an insulator.

If the *Pmmm* structure of GBCO is taken as reference, a few configurations have negative hydration enthalpies, suggesting possible hydration. However, if the tilted structure is taken as the reference state for perfect GBCO, all the hydration enthalpies become positive, suggesting an endothermic process. The calculations also show that protons would preferentially bind to oxygens of the $CoO_2$ plane. However, we point out that in the present calculations, hydration is unfavored by the strong elastic cost associated with the volume increase of the hydrated configurations.

We have completed this study by recomputing the C4 configuration using LDA+*U* instead of GGA+*U*, with the same

**Table 3** Hydration enthalpies $\Delta H_{hydr}$ (eV/$H_2O$) in the different configurations studied, computed either with respect to *Pmmm*, or with respect to the tilted structure of GBCO. These two original structures differ by 1.19 eV/38-atom supercell which explains the difference between the two columns. The protonic sites are those shown on Fig. 9. O3' denotes the oxygen atom added in the $GdO_{0.5}$ plane following water insertion.

| Concentration (% of filled O vacancies) | Plane | Configuration | $\Delta H_{hydr}$ (eV/$H_2O$) Ref: *Pmmm* | $\Delta H_{hydr}$ (eV/$H_2O$) Ref: tilted structure | Occupied protonic sites |
|---|---|---|---|---|---|
| 50% | BaO (Fig. 5) | B1 | -0.16 | 1.03 | O1-y, O2-x |
| | | B2 | 0.35 | 1.54 | O1-y, O2-y |
| | | B3 | 0.66 | 1.85 | O1-y, O2-y |
| | | B4 | -0.16 | 1.03 | O1-y, O2-x |
| | | B5 | 0.66 | 1.85 | O1-x, O2-x |
| | | B6 | 0.01 | 1.20 | O1-y, O2-x |
| 50% | $GdO_{0.5}$ (Fig. 7) | G1 | 0.13 | 1.32 | O3-x, O3'-y |
| | | G2 | 0.41 | 1.60 | O3-y, O3'-y |
| 50% | $GdO_{0.5}$ and $CoO_2$ (Fig. 7) | GC1 | 0.67 | 1.86 | O6-z1, O3'-y |
| | | GC2 | 0.67 | 1.86 | O4-z1, O3-x |
| 50% | $CoO_2$ (Fig. 6) | C1 | -0.59 | 0.60 | O4-y, O5-y |
| | | C2 | -0.12 | 1.07 | O5-z1, O4-z1 |
| | | C3 | 0.80 | 1.99 | O4-z2, O5-z2 |
| | | C4 | -0.63 | 0.56 | O6-z1, O4-z1 |
| 25% | $CoO_2$ (Fig. 8) | | -2.27 | 0.12 | O6-x, O6-x |

($U$,$J$). Using *Pmmm* as reference structure for GBCO, it provides $\Delta H_{hydr}$ = -0.77 eV/$H_2O$, close to the GGA result. Using the tilted structure as reference for GBCO, we find $\Delta H_{hydr}$ = -0.16 eV/$H_2O$, which remains negative (because the tilted structure of GBCO is more stable than *Pmmm* by only 0.61 eV/supercell in LDA versus 1.19 eV/supercell in GGA).

### 4.2 Hydration at lower water concentration

We now construct a 76-atom supercell, by doubling the previous 38-atom one along the $x$ direction. Then we introduce the two protonic defects, one in each half of the supercell (to minimize electrostatic repulsion), and add an oxygen atom in one of the vacancies. The hydration rate is thus half the ones studied in the previous subsection (the formula of the hydrated compound is now $GdBaCo_2O_{5.625}H_{0.25}$). The two protonic sites are chosen as being O6-x, because this site emerges as the most stable for the proton (see next section). A picture of the hydrated $CoO_2$ plane after structural optimization is shown on Fig. 8.

We obtain an hydration enthalpy of +0.12 eV/$H_2O$ with respect to the distorted structure (-2.27 eV with respect to *Pmmm*). $\Delta H_{hydr}$, calculated with respect to the distorted structure, remains a positive quantity, but we note that it is significantly decreased with respect to the enthalpies obtained at higher water concentration.

This result suggests that water insertion may be favored at low water concentration.

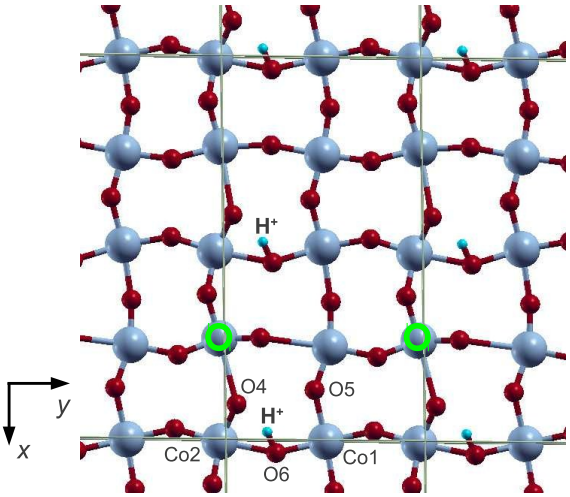


**Fig. 8** The $CoO_2$ plane containing the protons in the configuration with lower water concentration (25% of the oxygen vacancies are filled by the oxygens coming from $H_2O$). The green circles materialize the Co2 atoms above which is inserted the O atom coming from the $H_2O$ molecule. The grey lines are the supercell boundaries.

## 5 Protonic defects in GBCO

### 5.1 Formation enthalpy

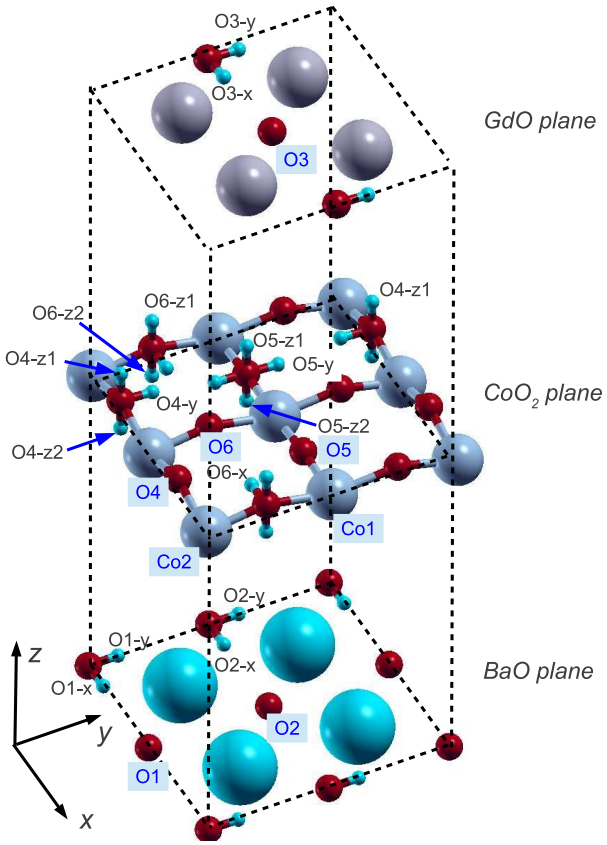


**Fig. 9** The different positions of the proton in the GBCO supercell. The BaO, $CoO_2$ and $GdO_{0.5}$ planes are spaced out for clarity.

We now investigate hydration at lower concentration by the simulation of single protonic defects in the GBCO supercell. In the 38-atom supercell, we add an H atom (bonded to an oxygen under the form of an OH group) in all the possible interstitial positions non equivalent by symmetry, and remove an electron from the supercell (a neutralizing uniform background is used, as usual in such computations). For each optimized configuration (atomic positions and supercell), we can define the formation enthalpy[57] of the protonic defect according to

$$\Delta H_f(H^+) = E_{tot}(GBCO+H^+) - E_{tot}(GBCO,ref) + \mu_e - \mu_H,$$

in which $E_{tot}(GBCO+H^+)$ is the total energy of the GBCO supercell with an hydrogen interstitial and an electron removed, and $E_{tot}(GBCO,ref)$ that of perfect GBCO in its reference structure (either *Pmmm* or the tilted one), all fully relaxed. $\mu_e = E_{VBM}^{ref} + \varepsilon_F$ is the electronic chemical potential, $E_{VBM}^{ref}$ the energy of the valence band maximum of the perfect reference structure (*Pmmm* or the tilted one), and $\varepsilon_F$ the Fermi level, that varies between 0 and the bandgap $E_g$. $\mu_H$ is the chemical potential of hydrogen. The valence band maximum $E_{VBM}$ is obtained by computing perfect GBCO with an electron removed, and substracting this total energy to that of perfect (neutral) GBCO: $E_{VBM} = E_{tot}(GBCO, q = 0) - E_{tot}(GBCO, q = 1)$. Before calculating these quantities, the total energies resulting from the charged supercell calculations are corrected by operating a band realignment[58] (this correction recovers the reference lost when the $G = 0$ component of the potential is arbitrarily set to zero in the calculation of the charged supercell). This realignment is performed by using as reference the deep semicore 3*s* levels of cobalt[59]. Using $2\mu_H + \mu_O = \mu_{H_2O}$, $\mu_H$ can be related to the oxygen and water chemical potentials, and then to the temperature and oxygen/water partial pressures, using empirical formulas[60,61]. Finally, we have

$$\Delta H_f(H^+) = E_{tot}(GBCO+H^+) - E_{tot}(GBCO,ref) + \mu_e - \frac{\mu_{H_2O} - \mu_O}{2} \quad (2)$$

In each case, the supercell is fully optimized (atomic positions and lattice constants). Note that these structural optimizations are performed with all the spatial symmetries broken to avoid relaxing to a local minimum. The protonic sites are shown on Fig. 9, and labeled according to the oxygen at which $H^+$ is bonded and by the direction of the OH group. The protonic formation enthalpies are computed for T=600 K, $P_{O_2}$ = 0.2 bar, $P_{H_2O}$ = 0.025 bar and $\varepsilon_F$ = 0 eV (oxidizing atmosphere), which roughly corresponds to the thermodynamic conditions of a PCFC cathode. They are plotted on Fig. 10.

The possible sites have very different formation enthalpies. Once again, their sign may depend on the reference structure chosen: in the case of *Pmmm*, several sites have a negative formation enthalpy. The formation enthalpies using the tilted structure as reference are higher, but not as high as 1.19 eV (energy difference between *Pmmm* and the tilted structure) because $E_{VBM}^{ref}$ is different for the two reference structures. A few configurations have negative formation enthalpy even if the distorted structure is taken as reference, suggesting possibility of hydration. This is probably related to the lowest elastic energy cost of the present configurations (the volume increase is only +1.1% for O6-x).

Note that $\Delta H_f < 0$ has no quantitative significance in the formalism of Zhang and Northrup[57], which assumes defects in the dilute limit (concentration $\propto e^{-\Delta H_f/k_BT} << 1$). In the present case, $\Delta H_f < 0$ simply means that formation of the protonic defect is spontaneous, and can be related to an exothermic hydration process.

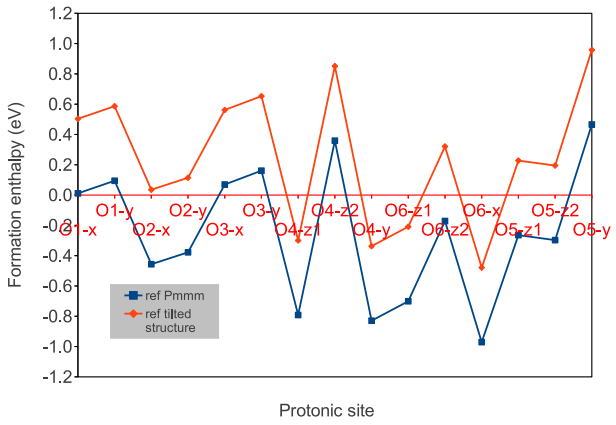


**Fig. 10** Formation enthalpy (eV) of the protonic defect in its different possible sites, computed for T=600 K, $P_{O_2}$ = 0.2 bar, $P_{H_2O}$ = 0.025 bar and $\varepsilon_F$ = 0 eV (oxidizing conditions), for the two reference structures of GBCO (*Pmmm* and the tilted structure).

### 5.2 Protonic energy landscape

In the BaO plane, two configurations (O2-x and O2-y) emerge as more stable than the others. In the $CoO_2$ plane, the most stable sites correspond, either to $H^+$ perpendicular to the plane and pointing towards $GdO_{0.5}$ (O4-z1, O6-z1), or lying in the plane (O4-y, O6-x) (Fig. 12). This last point corroborates the result of the previous section, in which the most stable hydrated configurations have their protons either lying in the $CoO_2$ plane, or bonded to oxygens of this plane and directed towards $GdO_{0.5}$: the previous C1 configuration corresponds to the combination of O4-y (very stable) and O5-y (unstable), while the previous C4 corresponds to the combination of O4-z1 and O6-z1. The high stability of these two sites explains the hydration enthalpy of C4. O4-z1, O4-y and O6-x are the three most stable sites and have very close energies.

The four most stable configurations have protons bonded to oxygens of the $CoO_2$ plane, either O4 or O6. The most stable site is O6-x. In this configuration, GBCO develops an antiferrodistortion in antiphase around the *c* axis, showed on Fig. 11-a, similar to that of the distorted structure of GBCO (Fig. 4). The OH is bonded to the nearest oxygen of the $CoO_2$ plane by an hydrogen bond of 1.68 Å (Fig. 11-b). O4-y, which is slightly less stable, exhibits the same kind of tilt motion, as well as O4-z1 and O6-z1.

In these protonic configurations, the charge states (+3) of the Co atoms is preserved. The Co ions are in the high-spin state, excepting in two cases (O1-y and O5-y), that correspond however to unstable configurations. The identification of stable sites allows anticipating a potential diffusion pathway as discussed in Sec. 7.

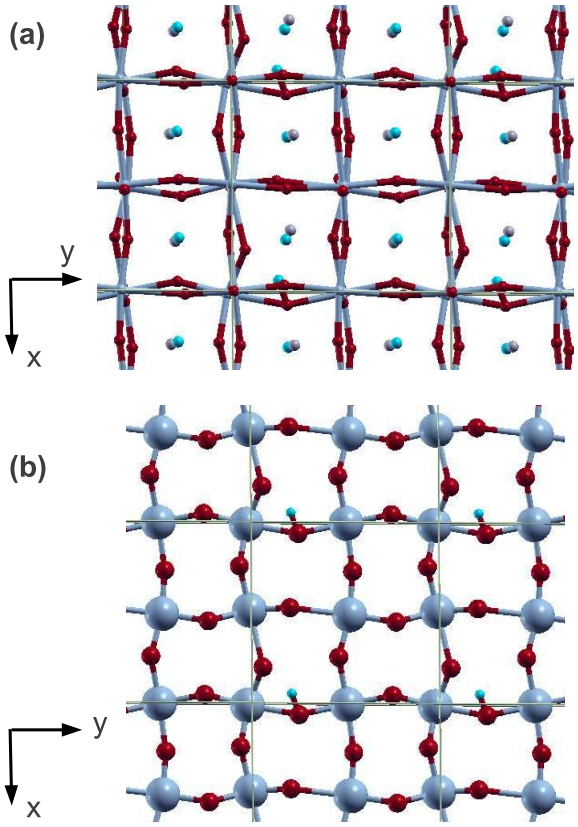


**Fig. 11** View of the most stable protonic configuration (O6-x). (a): whole structure (the antiferrodistortion is visisble); (b): the $CoO_2$ plane containing the protonic defect. The grey lines are the supercell boundaries.

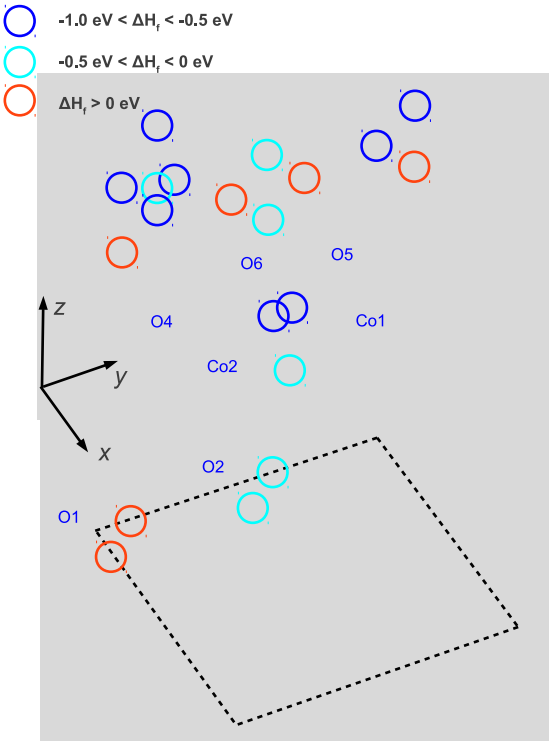


**Fig. 12** The different positions of the proton bonded to oxygens of the $CoO_2$ and BaO planes. The circles around the protons are colored according to the stability of the site (formation enthalpies at T=600 K, $P_{O_2}$=0.2 bar, $P_{H_2O}$=0.025 bar and $\varepsilon_F$ = 0 eV, taking *Pmmm* as the reference structure for perfect GBCO).

## 6 Oxidized and reduced configurations

We now investigate the possible reaction of GBCO with oxygen, i.e. oxygen insertion (oxidation) or removal (reduction).

### 6.1 Oxidation

Oxidation is simulated by adding an oxygen atom in one vacancy of the 38-atom supercell, leading to a compound with chemical formula $GdBaCo_2O_{5.75}$. Formally, this insertion produces two holes according to

$$1/2O_2 + \square_{\square}^{X} \rightarrow O_{\square}'' + 2h^{\bullet} \quad (3)$$

If *Pmmm* (resp. tilted) is used as reference structure for GBCO, and if the initial symmetries of the parent GBCO structure are kept during the optimization, the final oxidized configuration corresponds to an endothermic process, with oxidation enthalpy $\Delta H_{ox}$ = 0.45 (resp. 1.64) eV/O atom. If all the symmetries are broken, the system relaxes to a more stable – low-symmetry – state, with a negative (positive) oxidation enthalpy of -0.43 (resp. 0.76) eV/O atom, thus corresponding to an exothermic (resp. endothermic) process.

The optimized low-symmetry configuration exhibits, once again, a tilt of the oxygen octahedra in antiphase around the *c* axis. This is in agreement with experiments[12], showing that oxidized GBCO is associated with a tilt motion of the $CoO_6$ octahedra. In this oxidized configuration, the AFM order is perturbed (Fig. 13). The change of volume with respect to non oxidized *Pmmm* is +2.3%, which is inbetween O6-x (the most stable protonated site: +1.1%) and the hydrated C4 configuration (+5.6%).

The resulting compound has rather the electronic structure of a *p*-type metal, with empty states appearing within the bandgap, rather well separated from the top of the valence band (Fig. 13). Since states of the valence band top are rather of oxygen-type[1], the holes produced by this oxidation are probably mainly localized on oxygen atoms, even though a perturbation of the electronic state of some $Co^{3+}$ ions can not be excluded due to the presence of cobalt 3*d* states close to the top of the valence band (Fig. 3). In the final oxidized configuration, indeed, two Co ions have their magnetic moment decreased to $\sim 2.8\ \mu_B$, but the number of *d* electrons does not change with respect to the perfect configuration. It is important to note that the oxygen 2*p*-type character of the valence band top is mainly the consequence of the high-spin state of the $Co^{3+}$ ion, since Hund exchange contributes to deeply stabilize the occupied Hubbard subband corresponding to the majority spin channel. If some of the $Co^{3+}$ ions were in lower spin state (IS or LS), it is probable that their *d* orbitals would contribute more to the highest occupied states, and in that case, $Co^{4+}$ ions could appear in oxidizing conditions. Knizek et

al.[49] have illustrated this point by computing the electronic structure of $LaCoO_3$ in various spin states for $Co^{3+}$.

The question is whether the present GGA+$U$ functional is able to correctly describe such holes or not. In fact, holes in charge-transfer metal oxides are usually observed to be oxygen-type hole polarons, and their modeling by DFT has been the subject of intensive research. It is commonly admitted that such holes are localized on one oxygen atom[62–65], formally $O^-$ (self-trapped oxygen-type small polaron), and that standard GGA applied to the 2$p$ states of oxygen is not able to describe the self-trapping of such holes (only trapping by a defect can be reached with such functionals[66,67]). A Hubbard correction on the 2$p$ states of oxygen is usually mandatory to describe the self-trapped oxygen hole polarons[63,64].

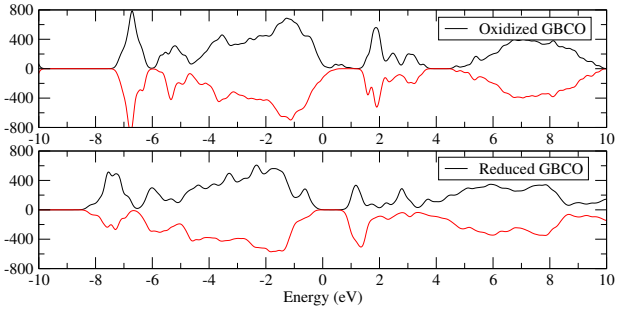


**Fig. 13** Density of states (arb. units) of (i) $GdBaCo_2O_{5.75}$ (oxidized GBCO, low-symmetry configuration), (ii) $GdBaCo_2O_{5.25}$ (reduced GBCO) in the O3 configuration (oxygen removed from the $GdO_{0.5}$ plane).

### 6.2 Reduction

Reduction is simulated by removing one oxygen atom from the supercell. Six possible configurations, corresponding to the six nonequivalent oxygens, have been studied, here again with and without the symmetries of the parent GBCO structure. This leads to a compound with chemical formula $GdBaCo_2O_{5.25}$. Formally, this removal produces two electrons according to

$$O_O^X \rightarrow V_O^{\bullet\bullet} + 1/2O_2 + 2e^{'} \quad (4)$$

However, the two electrons do not delocalize over the crystal in a conduction band state. Since the bottom of the conduction band is made of Co 3$d$ states (Fig.3), they strongly localize and reduce two cobalt into $Co^{2+}$ ions, according to

$$V_O^{\bullet\bullet} + 2e^{'} + 2Co_{Co}^X \rightarrow V_O^{\bullet\bullet} + 2Co_{Co}^{'} \quad (5)$$

At the same time, the energy of the newly occupied 3$d$ states decrease, cross the gap, and join the valence band top, as a consequence of the strong electronic correlations affecting the 3$d$ orbitals of Co. The resulting compound is thus an insulator at T=0 K, in good agreement with experiments[40]. The reduction of two Co ions in the supercell is directly visible on the magnetic moments: two Co ions have their magnetic moment decreased to $\sim 2.6\ \mu_B$ (value typical of the $Co^{2+}$ ion in high-spin configuration[30]), while all the others keep a magnetic moment of $\sim$ 2.95-3.1 $\mu_B$, still corresponding to $Co^{3+}$ ion in high-spin state. Moreover, the number of $d$ electrons on the reduced Co slightly increases with respect to the other $Co^{3+}$ ions.

The process is found endothermic in all cases, with a reduction enthalpy $\Delta H_{red} > 0$, depending on the oxygen atom removed (see Tab. 4). The most unfavorable sites for reducing GBCO are the two oxygens of the BaO plane (O1, O2). The most favorable one is the oxygen of the $GdO_{0.5}$ plane (in qualitative agreement with Ref.[68]), with a +0.15/1.34 eV/O atom enthalpy depending on the structure chosen as reference for GBCO (*Pmmm*/tilted). In this reduced configuration, the AFM order is perturbed (Fig. 13), but no tilt system appears.

## 7 Discussion

### 7.1 Possible migration paths of protons

Predicting the migration paths of protons would require to compute energy barriers between the stable sites, which is out of the scope of the present study. However, it is possible to infer these paths by examining the protonic energy landscape, and by searching for possible paths passing only through stable or very stable sites:

(i) along $a$: a path exists passing through the sites attached to oxygens O4 and O6 in the $CoO_2$ plane, namely: O4-y $\rightarrow$ O6-x $\rightarrow$ O6-z1 $\rightarrow$ O6-x $\rightarrow$ O4-y, involving the traditional succession of hopping and reorientation motions of the OH group. This path joins only very stable sites and is thus probably very favorable.

(ii) along $b$: it is more difficult for the proton to diffuse along $b$ because the O5 oxygens are associated with unstable sites (O5-y). However, these sites could be circumvented by passing by the O2-x and O2-y sites of the BaO plane, which would involve only stable or very stable sites, as: O4-y $\rightarrow$ O6-x $\rightarrow$ O6-z2 $\rightarrow$ O2-y $\rightarrow$ O2-x $\rightarrow$ O2-y $\rightarrow$ O6-z2 $\rightarrow$ O6-x $\rightarrow$ O4-y (keeping in mind that the ($a$,$b$) distinction disappears at $\sim$475°C).

(iii) along $c$: diffusion along $c$ must necessarily pass by the sites attached to the O3, which are both of high energy. This path thus probably exhibits high barriers.

Based on these arguments, protonic diffusion in GBCO can be expected to be very anisotropic, with probably favorable paths along $a$ and $b$, not along $c$.

**Table 4** Oxidation enthalpy, and reduction enthalpies in the oxygen different sites (in eV/O atom). O1 ... O6 correspond to the oxygen atom removed. The asterix corresponds to the enthalpy computed under the constraint of symmetries of *Pmmm* GBCO with the O atom added or removed. O3' is the oxygen added in the $GdO_{0.5}$ plane.

| Oxidation | Plane | Oxygen added | Oxidation enthalpy $\Delta H_{ox}$ (eV/O atom) Ref: *Pmmm* | Oxidation enthalpy $\Delta H_{ox}$ (eV/O atom) Ref: tilted structure |
|---|---|---|---|---|
| | $GdO_{0.5}$ plane | O3' | +0.45* | 1.64* |
| | | | -0.43 | 0.76 |
| **Reduction** | **Plane** | **Oxygen removed** | **Reduction enthalpy $\Delta H_{red}$ (eV/O atom) Ref: *Pmmm*** | **Reduction enthalpy $\Delta H_{red}$ (eV/O atom) Ref: tilted structure** |
| | BaO plane | O1 | 1.72* | 2.91* |
| | | | 1.42 | 2.61 |
| | | O2 | 2.62* | 3.81* |
| | | | 1.32 | 2.51 |
| | $GdO_{0.5}$ plane | O3 | 0.19* | 1.38* |
| | | | 0.15 | 1.34 |
| | $CoO_2$ plane | O4 | 0.71* | 1.90* |
| | | | 0.50 | 1.69 |
| | | O5 | 0.25* | 1.44* |
| | | O6 | 0.68 | 1.87 |

### 7.2 Oxidation and reduction

Our results on the oxidized/reduced system can be directly compared to the experimental results of Taskin et al[40], who studied the electrical and magnetic behavior of $GdBaCo_2O_{5+x}$, $0 \leq x \leq 0.77$. The temperature/oxygen content phase diagram of GBCO proposed by these authors shows that at very low temperature, the compound remains an antiferromagnetic insulator for all the oxygen contents studied. Moreover the conductivity exhibits a very asymmetric profile as a function of oxygen content around 0.5, the system tending to be insulating for $x \leq 0.5$ (reduction) and conductor for $x \geq 0.5$ (oxidation)[69]. We add that the resistivity decreases with temperature in both cases[69] (oxidation and reduction), suggesting a thermally activated mechanism of charge transport involving probably small polaron hopping.

For $x \leq 0.5$, this is in good agreement with our results, since we have obtained an insulating reduced compound, owing to the localization of the electrons released by oxygen removal (formation of $Co^{2+}$).

For $x \geq 0.5$, we have obtained a *p*-type metallic electronic structure. Although the transition to the metal, after the experimental study of Taskin et al[40], should occur beyond $x \sim$ 0.85-0.90, the appearance of holes at the top of the valence band in our calculation suggests a decrease in the resistivity that corroborates the experimental tendency. Taskin et al[69] associate the oxidized state to the formation of $Co^{4+}$ ions. Our density-functional approach rather suggests the formation of O-type hole polarons, or at least states with a mixed oxygen $2p$ - cobalt $3d$ character, as suggested by the partial density of states (Fig. 3). However, as already stated, this is certainly the consequence of the high-spin state of the $Co^{3+}$ ion found in the present calculations. Lower spin states (IS, LS) of $Co^{3+}$, as suggested by many experimental works at intermediate temperatures, could favor the formation of $Co^{4+}$ ions in oxidized environments.

Finally, reduction is found in all cases as an endothermic process. Oxidation also if the tilted structure of GBCO is used as reference.

## 8 Conclusion

In the present work, we have investigated within GGA-PBE+*U* the crystal structure, magnetism and electronic structure, as well as the hydration, oxidation and reduction reactions of double cobaltite $GdBaCo_2O_{5.5}$.

Among the different spin configurations tested, the most stable found corresponds to HS on all the Co ions. A structure more stable than *Pmmm* has been found, with a tilt of the oxygen octahedra/pyramids around the *c* axis.

Hydrated configurations have been studied. The most stable ones correspond to protons bonded to oxygens of the $CoO_2$ plane, and exhibit strong structural distortions, in particular tilts in antiphase around the *c* axis. Based on the computed protonic energy landscape, migration paths of protons in the

$CoO_2$ plane have been suggested. Hydration in several configurations with high water content (50% of the vacancies filled) has been found exothermic if *Pmmm* is taken as reference, but always endothermic if the distorted structure is taken as reference, at least in GGA+$U$ (LDA+$U$ provides a slightly exothermic reaction). However, the hydration enthalpy decreases significantly if water content is reduced (+0.12 eV at 25% of the vacancies filled), suggesting that hydration might become possible at low water concentration, i.e. when the elastic cost of insertion is low enough. Moreover, the formation of protonic defects is found exothermic in several configurations.

In its reduced state, GBCO is an insulator, as a consequence of the strong electronic correlations affecting the 3$d$ electrons of cobalt ($Co^{3+} + e^{'} \rightarrow Co^{2+}$). Reduction is endothermic. The most favorable site for oxygen removal is in the $GdO_{0.5}$ plane.

In the oxidized state, by contrast, GBCO is found rather metallic ($p$-type). Although our theoretical scheme may suffer from the difficulty of GGA-PBE to describe correctly a localized 2$p$ state (oxygen-type self-trapped hole polaron, $O^{-}$), this is in rather good agreement with measurements of electrical conductivity in $GdBaCo_2O_{5+x}$, that exhibit a strong asymmetry with respect to $x = 0.5$.

## 9 Acknowledgements

This work was supported by the Agence Nationale de la Recherche through the IDEA-MAT project (ANR-12-BS08-0012-01). The calculations have been performed on the TERA-100 supercomputing center of CEA/DAM. B. Amadon is acknowledged for fruitful discussions.

## 10 Appendix

### 10.1 Structural data

In Tab. 5 are given the optimized atomic positions obtained in two theoretical schemes:

(i) GGA+$U$: $(U_{3d}^{Co}, J_{3d}^{Co})$=(5,0) eV and Gd 4$f$ electrons frozen in the core;

(ii) GGA+$U$: $(U_{3d}^{Co}, J_{3d}^{Co})$=(5,0) eV and $(U_{4f}^{Gd}, J_{3d}^{Co})$=(5,0) eV.

### 10.2 Influence of theoretical scheme ($U$,$J$) and magnetic order

In order to evaluate the role of Hubbard parameter $U_{3d}^{Co}$ and exchange coupling $J_{3d}^{Co}$ in the present study, we recompute the hydration enthalpy in the C4 configuration, i.e. we fully optimize perfect GBCO and the hydrated system using different $(U_{3d}^{Co}, J_{3d}^{Co})$. For these tests, we use *Pmmm* as the reference structure for perfect GBCO. We find that the hydration enthalpy does not vary significantly from $U_{3d}^{Co}$=4 eV to 6 eV (see Tab. 6).

| Numerical scheme | Hydration enthalpy | Magnetic order |
|---|---|---|
| Gd 4$f$ frozen in the core | | |
| $U_{3d}^{Co}$=4 eV, $J_{3d}^{Co}$= 0 eV | -0.76 | Co: AFM3 |
| $U_{3d}^{Co}$=5 eV, $J_{3d}^{Co}$= 0 eV | -0.63 | Co: AFM3 |
| $U_{3d}^{Co}$=6 eV, $J_{3d}^{Co}$= 0 eV | -0.84 | Co: AFM3 |
| $U_{3d}^{Co}$=5 eV, $J_{3d}^{Co}$= 0 eV | -1.15 | Co: AFM2 |
| $U_{3d}^{Co}$=5 eV, $J_{3d}^{Co}$= 1 eV | -1.42 | Co: AFM2 |
| $U_{3d}^{Co}$=5 eV, $J_{3d}^{Co}$= 0 eV | -1.38 | Co: AFM1 |
| $U_{3d}^{Co}$=5 eV, $J_{3d}^{Co}$= 1 eV | -0.96 | Co: AFM1 |
| Gd 4$f$ treated in the valence | | |
| $U_{3d}^{Co}$=5 eV, $J_{3d}^{Co}$= 0 eV | -0.56 | Co: AFM3 |
| $U_{4f}^{Gd}$=5 eV, $J_{4f}^{Gd}$= 0 eV | | Gd: FM |

**Table 6** Hydration enthalpy (eV/$H_2O$) in the C4 configuration using different numerical schemes and different antiferromagnetic orders. For the AFM1 and AFM2 cases, the hydration enthalpy is computed under the assumption that the AFM order is the same in the dry and hydrated configurations. The reference structure of perfect GBCO for the calculation of the hydration enthalpy is *Pmmm*.

The two AFM1 and AFM2 orders have also been tested, i.e. we recompute the hydrated system using these two magnetic configurations, using $U_{3d}^{Co}$=5 eV and $J_{3d}^{Co}$=0 or 1 eV. In all cases, the hydration enthalpy is obtained negative with respect to *Pmmm*.

### 10.3 Direct treatment of 4$f$ electrons of Gd in the valence

We also test the direct treatment of the Gd 4$f$ electrons in the valence and recompute the hydrated C4 configuration. The Gd 4$f$ are assumed as ferromagnetically coupled with each other, while the Co ions remain antiferromagnetically coupled (AFM3), so that the total spin magnetic moment of the supercell, which contains 4 $Gd^{3+}$ ions, is 28 $\mu_B$. Using also the total energy of the perfect GBCO supercell computed in the same manner, the hydration enthalpy is -0.56 eV/$H_2O$ (Tab. 6), close to the -0.63 eV obtained when the 4$f$ electrons are frozen in the core (here again, *Pmmm* is used as the reference structure for perfect GBCO).

## References

1 H. Wu, J. Phys.: Cond. Matt. **15**, 503 (2003).

2 A. Chroneos, B. Yildiz, A. Tarancon, D. Parfitt, J. A. Kilner, Energy and Environmental Science **4**, 2774 (2011).

3 A. Tarancon, A. Morata, G. Dezanneau, S. J. Skinner, J. A. Kilner, S. Estrade, F. Hernandez-

| Co3$d$ | Gd 4$f$ | $y_{Ba}$ | $y_{Gd}$ | $z_{Co1}$ | $z_{Co2}$ | $z_{O4}$ | $z_{O5}$ | $y_{O6}$ | $z_{O6}$ |
|---|---|---|---|---|---|---|---|---|---|
| $(U_{3d}^{Co},J_{3d}^{Co})$=(5,0) | core | 0.2558 | 0.2694 | 0.2555 | 0.2481 | 0.3157 | 0.2746 | 0.2384 | 0.2980 |
| $(U_{3d}^{Co},J_{3d}^{Co})$=(5,0) | $(U_{4f}^{Gd},J_{3d}^{Co})$=(5,0) | 0.2566 | 0.2680 | 0.2546 | 0.2460 | 0.3133 | 0.2712 | 0.2383 | 0.2943 |
| Expt[53] | | 0.2498 | 0.2722 | 0.2510 | 0.2553 | 0.3016 | 0.2764 | 0.24472 | 0.2905 |

**Table 5** Atomic positions for $GdBaCo_2O_{5.5}$ (*Pmmm* space group) in the AFM3 antiferromagnetic state, using several theoretical schemes, and compared to experiments.


Ramirez, F. Peiro, J.-R. Morante, Journal of Power Sources **174**, 255 (2007).

4 B. Wei, Z. Lu, W. Jiang, X. Zhu, W. Su, Electrochimica Acta **134**, 136 (2014).

5 A. C. Tomkiewicz, M. Meloni, S. McIntosh, Solid State Ionics **260**, 55 (2014).

6 Y. Lee, D. Y. Kim, G. M. Choi, Solid State Ionics **192**, 527 (2011).

7 N. Li, Z. Lu, B. Wei, X. Huang, K. Chen, Y. Zhang, W. Su, Journal of Alloys and Compounds **454**, 274 (2008).

8 A. Tarancon, D. Marrero-Lopez, J. Pena-Martinez, J.-C. Ruiz-Morales, P. Nunez, Solid State Ionics **179**, 611 (2008).

9 A. Tarancon, J. Pena-Martinez, D. Marrero-Lopez, A. Morata, J.-C. Ruiz-Morales, P. Nunez, Solid State Ionics **179**, 2372 (2008).

10 Y. Hu, C. Bogicevic, Y. Bouffanais, M. Giot, O. Hernandez, G. Dezanneau, Journal of Power Sources **242**, 50-56 (2013).

11 M.-H. Ko, Y.-S. Yoo, J.-H. Hwang, Ceramics International **41**, 4616 (2015).

12 D. Munoz-Gil, D. Perez-Coll, J. Pena-Martinez, S. Garcia-Martin, Journal of Power Sources **263**, 90 (2014).

13 D. Parfitt, A. Chroneos, A. Tarancon, J. A. Kilner, J. Mat. Chem. **21**, 2183 (2011).

14 J. Hermet, G. Geneste, G. Dezanneau, Appl. Phys. Lett. **97**, 174102 (2010).

15 A. Chroneos, D. Parfitt, R. V. Vovk, I. L. Goulatis, Mod. Phys. Lett. B **26**, 1250196 (2012).

16 I. D. Seymour, A. Tarancon, A. Chroneos, D. Parfitt, J. A. Kilner, R. W. Grimes, Solid State Ionics **216**, 41 (2012).

17 J. Hermet, B. Dupé, G. Dezanneau, Solid State Ionics **216**, 50-53 (2012).

18 Y. Hu, O. Hernandez, T. Broux, M. Bahout, J. Hermet, A. Ottochian, C. Ritter, G. Geneste, G. Dezanneau, Journal of Materials Chemistry **22** 18744-18747 (2012).

19 H. Shiiba, M. Nakayama, T. Kasuga, R. W. Grimes, J. A. Kilner, Phys. Chem. Chem. Phys. **15**, 10494 (2013).

20 G. Goupil, T. Delahaye, B. Sala, F. Lefebvre Joud, G. Gauthier, Solid State Ionics **263**, 15 (2014).

21 M. Allieta, M. Scavini, L. Lo Presti, M. Coduri, L. Loconte, S. Capelli, C. Oliva, P. Ghigna, P. Pattison, V. Scagnoli, Phys. Rev. B **88**, 214104 (2013).

22 L. V. Nomerovannaya, A. A. Makhnev, S. V. Streltsov, I. A. Nekrasov, M. A. Korotin, S. V. Shiryaev, G. L. Bychkov, S. N. Barilo, V. I. Anisimov, J. Phys.: Cond. Matt. **16**, 5129 (2004).

23 J. Chen, A. Selloni, Phys. Rev. B **85**, 085306 (2012).

24 J. Chen, X. Wu, A. Selloni, Phys. Rev. B **83**, 245204 (2011).

25 Y. S. Meng, A. Van Der Ven, M. K. Y. Chan, G. Ceder, Phys. Rev. B **72**, 172103 (2005).

26 F. Zhou, M. Cococcioni, C. A. Marianetti, D. Morgan, G. Ceder, Phys. Rev. B **70**, 235121 (2004).

27 A. Rebola, R. Klie, P. Zapol, S. Ögüt, Phys. Rev. B **85**, 155132 (2012).

28 M. J. Han, H.-S. Kim, D. G. Kim, J. Yu, Phys. Rev. B **87**, 184432 (2013).

29 S. Grytsyuk, M. V. Peskov, U. Schwingenschlögl, Phys. Rev. B **86**, 174115 (2012).

30 M. M. Markina, B. V. Mill, E. A. Zvereva, A. V. Ushakov, S. V. Streltsov, A. N. Vasiliev, Phys. Rev. B **89**, 104409 (2004).

31 V. Pardo, D. Baldomir, Phys. Rev. B **73**, 165117 (2006).

32 Q. Zhang, W. Zhang, Phys. Rev. B **67**, 094436 (2003).

33 H. Wu, Phys. Rev. B **64**, 092413 (2001).

34 K. Conder, E. Pomjakushina, V. Pomjakushin, M. Stingaciu, S. Streule, A. Podlesnyak, J. Phys.: Cond. Matt. **17**, 5813 (2005).

35 W. R. Flavell, A. G. Thomas, D. Tsoutsou, A. K.

Mallick, M. North, E. A. Seddon, C. Cacho, A. E. R. Malins, S. Patel, R. L. Stockbauer, R. L. Kurtz, P. T. Sprunger, S. N. Barilo, S. V. Shiryaev, G. L. Bychkov, Rev. B **70**, 224427 (2004).

36 C. Frontera, J. L. Garcia-Munoz, A. Llobet, M. A. G. Aranda, Phys. Rev. B **65**, R180405 (2002).

37 Y. Moritomo, T. akimoto, M. Takeo, A. Machida, E. Nishibori, M. Takata, M. Sakata, K. Ohoyama, A. Nakamura, Phys. Rev. B **61**, R13325 (2000).

38 A. Maignan, C. Martin, D. Pelloquin, N. Nguyen, B. Raveau, J. Solid State Chem. **142**, 247 (1999).

39 M. Garcia-Fernandez, V. Scagnoli, U. Staub, A. M. Mulders, M. Janousch, Y. Bodenthin, D. Meister, B. D. Patterson, A. Mirone, Y. Tanaka, T. Nakamura, S. Grenier, Y. Huang, K. Conder, Phys. Rev. B **78**, 054424 (2008).

40 A. A. Taskin, A. N. Lavrov, Y. Ando, Phys. Rev. B **71**, 134414 (2005).

41 W. Kohn and L. J. Sham, Phys. Rev. **140**, A1133 (1965).

42 X. Gonze, J.-M. Beuken, R. Caracas, F. Detraux, M. Fuchs, G.-M. Rignanese, L. Sindic, M. Verstraete, G. Zerah, F. Jollet, M. Torrent, A. Roy, M. Mikami, Ph. Ghosez, J.-Y. Raty, D.C. Allan. Computational Materials Science **25**, 478-492 (2002).

43 X. Gonze, G.-M. Rignanese, M. Verstraete, J.-M. Beuken, Y. Pouillon, R. Caracas, F. Jollet, M. Torrent, G. Zerah, M. Mikami, Ph. Ghosez, M. Veithen, J.-Y. Raty, V. Olevano, F. Bruneval, L. Reining, R. Godby, G. Onida, D.R. Hamann, and D.C. Allan. Z. Kristallogr. **220**, 558-562 (2005).

44 M. Torrent, F. Jollet, F. Bottin, G. Zérah and X. Gonze, Comput. Mat. Sci., **42** (2008), 337-351.

45 J. P. Perdew, K. Burke, and M. Ernzerhof, Phys. Rev. Lett. **77**, 3865 (1996).

46 E. Bevillon, J. Hermet, G. Dezanneau, G. Geneste, J. Mat. Chem. A **2**, 460 (2014).

47 S. Ganorkar, K. R. Priolkar, Solid State Comm. **150**, 1963 (2010).

48 G. Jomard, B. Amadon, F. Bottin, M. Torrent, Phys. Rev. B **78**, 075125 (2008).

49 K. Knizek, Z. Jirak, J. Hejtmanek, P. Novak, W. Ku, Phys. Rev. B **79**, 014430 (2009).

50 H. Hsu, P. Blaha, R. M. Wentzcovitch, Phys. Rev. B **85**, 140404(R) (2012).

51 T. Jia, H. Wu, G. Zhang, X. Zhang, Y. Guo, Z. Zeng, H.-Q. Lin, Phys. Rev. B **83**, 174433 (2011).

52 M. Respaud, C. Frontera, J.-L. Garcia-Munoz, M. A. G. Aranda, B. Raquet, J.-M. Broto, H. Rakoto, M. Goiran, A. Llobet, J. rodriguez-Carjaval, Phys. Rev. B **64**, 214401 (2001).

53 A. Tarancon, S. J. Skinner, R. J. Chater, F. Hernandez-Ramirez, J. A. Kilner, J. Mat. Chem. **17**, 3175 (2007).

54 Z. Hu, H. Wu, T. C. Koethe, S. N. Barilo, S. V. Shiryaev, G. L. Bychkov, C. Schüβler-Langeheine, T. Lorenz, A. Tanaka, H. H. Hsieh, H.-J. Lin, C. T. Chen, N. B. Brookes, S. Agrestini, Y.-Y. Chin, M. Rotter, L. H. Tjeng, New Journal of Physics **14**, 123025 (2012).

55 N. Ishizawa, T. Asaka, T. Kudo, K. Fukuda, N. Abe, T. Arima, J. Solid. State. Chem. **198**, 532 (2013).

56 Y. P. Chernenkov, V. P. Plakhty, V. I. Fedorov, S. N. Barilo, S. V. Shiryaev, G. L. Bychkov, Phys. Rev. B **71**, 184105 (2005).

57 S. B. Zhang and J. E. Northrup, Phys. Rev. Lett. **67**, 2339 (1991).

58 S. Lany, A. Zunger, Phys. Rev. B **78**, 235104 (2008).

59 A. Zywietz, J. Furthmüller, and F. Bechstedt, Phys. Rev. B **59**, 15166 (1999).

60 T. R. Paudel, S. S. Jaswal, E. Y. Tsymbal, Phys. Rev. B **85**, 104409 (2012).

61 D. R. Lide, ed., CRC Handbook of Chemistry and Physics, CRC Press, 2004-2005.

62 P. Erhart, A. Klein, D. Aberg, B. Sadigh, Phys. Rev. B **90**, 035204 (2014).

63 N. A. Deskins, M. Dupuis, J. Phys. Chem. C **113**, 346 (2009).

64 N. A. Deskins, M. Dupuis, Phys. Rev. B **75**, 195212 (2007).

65 J. B. Varley, A. Janotti, C. Franchini, C. G. Van De Walle, Phys. Rev. B **85**, 081109(R) (2012).

66 E. Bevillon, G. Dezanneau, G. Geneste, Phys. Rev. B **83**, 174101 (2011).

67 J. Hermet, F. Bottin, G. Dezanneau, G. Geneste, Phys. Rev. B **85**, 205137 (2012).

68 I. D. Seymour, A. Chroneos, J. A. Kilner, R. W. Grimes, Phys. Chem. Chem. Phys. **13**, 15305 (2011).

69 A. A. Taskin, Y. Ando, Phys. Rev. Letters **95**, 176603 (2005).